



High-resolution Spectroscopy of SN 2023ixf’s First Week: Engulfing the Asymmetric Circumstellar Material

Nathan Smith¹ , Jeniveve Pearson¹ , David J. Sand¹ , Ilya Ilyin² , K. Azalee Bostroem^{1,3} , Griffin Hosseinzadeh¹ , and Manisha Shrestha¹

¹ Steward Observatory, University of Arizona, 933 N. Cherry Avenue, Tucson, AZ 85721, USA

² Leibniz-Institut für Astrophysik Potsdam (AIP), An der Sternwarte 16, D-14482 Potsdam, Germany

Received 2023 June 13; revised 2023 July 26; accepted 2023 August 15; published 2023 October 6

Abstract

We present a series of high-resolution echelle spectra of SN 2023ixf in M101, obtained nightly during the first week or so after discovery using PEPSI on the Large Binocular Telescope. Na I D absorption in these spectra indicates a host reddening of $E(B - V) = 0.031$ mag and a systemic velocity of $+7 \text{ km s}^{-1}$ relative to the average redshift of M101. Dramatic changes are seen in the strength and shape of strong emission lines emitted by circumstellar material (CSM), including He II $\lambda 4686$, C IV $\lambda\lambda 5801, 5811$, H α , and N IV $\lambda\lambda 7109, 7123$. In general, these narrow lines broaden to become intermediate-width lines before disappearing from the spectrum within a few days, indicating a limited extent to the dense CSM of around 20–30 au (or $\lesssim 10^{14.7}$ cm). H α persists in the spectrum for about a week as an intermediate-width emission line with P Cyg absorption at 700–1300 km s^{-1} arising in the post-shock shell of swept-up CSM. Early narrow emission lines are blueshifted and indicate an expansion speed in the pre-shock CSM of about 115 km s^{-1} , but with even broader emission in higher-ionization lines. This is faster than the normal winds of red supergiants, suggesting some mode of eruptive mass loss from the progenitor or radiative acceleration of the CSM. A lack of narrow blueshifted absorption suggests that most of the CSM is not along our line of sight. This and several other clues indicate that the CSM of SN 2023ixf is significantly aspherical. We find that CSM lines disappear after a few days because the asymmetric CSM is engulfed by the supernova photosphere.

Unified Astronomy Thesaurus concepts: [Circumstellar matter \(241\)](#); [Supernovae \(1668\)](#)

1. Introduction

Understanding the late evolution and end fates of massive stars remains an enduring challenge. It was recognized long ago that mass loss plays a key role in determining the outcome of stellar evolution (Paczynski 1971; Chiosi & Maeder 1986). In recent years, however, the traditional view, where well-behaved, steady stellar winds of single stars lead to predictable outcomes with reliable metallicity-dependence (e.g., Heger et al. 2003), has gradually been eroding, giving way instead to a more complicated picture where binary interaction and eruptive events dominate the mass loss (see Smith 2014 for a review). These modes of mass loss do not have well-established monotonic trends with initial mass or metallicity, and are challenging for models of single-star evolution.

A major reason for this shifting paradigm is that normal, steady stellar winds of hot massive stars are evidently not as strong as we used to think, reducing their ability to remove the H envelope and to strongly impact the evolution (Smith & Owocki 2006; Puls et al. 2008; Smith 2014; Sundqvist et al. 2019). The same applies to red supergiant (RSG) winds, indicated by recent downward revisions of normal RSG wind mass-loss rates and the general scarcity of dust-enshrouded RSGs (Beasor et al. 2020; Beasor & Smith 2022). This shift is also influenced by results from several different lines of inquiry: (1) strong evidence for binary-stripped

progenitors of H-poor supernovae (SNe; Podsiadlowski et al. 1992; Drout et al. 2011; Smith et al. 2011), (2) observational evidence for extreme, eruptive modes of mass loss (Smith & Owocki 2006), and (3) firmer observational estimates of a high interacting binary fraction among O-type stars (Sana et al. 2012).

Another driving factor toward a more complicated view of mass loss has been the discovery of a number of different explosive transients that simply do not fit predictions of the traditional view of a massive star evolution dominated by single-star wind mass loss. Chief among these are SNe with signatures of strong shock interaction with circumstellar material (CSM). Evolved massive stars that retain their H envelopes usually have large radii and relatively slow escape speeds, which can lead to slow CSM that produces narrow H lines in the spectrum of the SN. In this case, they are classified as Type IIn (Schlegel 1990). The illumination or shock heating of close-in CSM can provide unique clues about the mass-loss properties of the progenitor star in the late evolutionary phases of its life, which are otherwise difficult to infer (see Smith 2017, for a review). There is wide diversity among SNe with observed signatures of H-rich CSM interaction, ranging from superluminous SNe IIn, scaling down through normal SNe IIn, and down to those with barely any observable signatures of CSM interaction.

On the less extreme end, we see interacting SNe where the spectral signatures of CSM interaction are fleeting. One of these events is the topic of the current paper. The narrow lines may last for only a few days or a week before fading, and they can quickly transition to look like normal⁴ SNe. This class of

³ LSSTC Catalyst Fellow.

Original content from this work may be used under the terms of the [Creative Commons Attribution 4.0 licence](#). Any further distribution of this work must maintain attribution to the author(s) and the title of the work, journal citation and DOI.

⁴ Normal here means a visual-wavelength spectrum dominated by an ejecta photosphere, not by CSM interaction.

objects has been known for about four decades. Well-studied examples of the phenomenon include SN 1983K (Niemela et al. 1985), SN 1993J (Benetti et al. 1994; Garnavich & Ann 1994), SN 1998S (Shivvers et al. 2015), SN 2006bp (Quimby et al. 2007), PTF11iqb (Smith et al. 2015), and SN 2013cu (Gal-Yam et al. 2014; Groh 2014; Gräfener & Vink 2016). Additional events studied in detail include SN 2013fs, SN 2017ahn, SN 2020pni, and SN 2020tlf (Bullivant et al. 2018; Tartaglia et al. 2021; Jacobson-Galán et al. 2022; Terreran et al. 2022). Because study of this class requires early discovery on timescales of hours or days after explosion, early examples were limited to fortuitous early detections of nearby events. With more systematic transient searches and early discovery becoming more routine, growing samples of this class have been identified (Khazov et al. 2016). Some estimates suggest that a large fraction ($\gtrsim 1/3$) of otherwise normal core-collapse SNe (ccSNe) have these early CSM features (Bruch et al. 2021), which is larger than the 8%–9% of ccSNe that are more traditional strongly interacting SNe IIn (Smith et al. 2011).

The defining characteristic of this class is very short-lived (a few days) narrow emission lines in the spectrum, which are thought to result from dense and confined CSM within 10 s of au around the progenitor star. As with the broader class of SNe IIn, this is a phenomenon that is not unique to any one type of explosion or any unique progenitor type because it depends on the characteristics of the surrounding material—in principle, any SN type might be surrounded by dense and confined CSM. In practice, the observed events tend to be H-rich (perhaps because narrow lines require that a progenitor had slow escape speeds due to a large H envelope), and they usually evolve into SNe I Ib, II-P, or II-L when the CSM interaction signatures fade. Early spectra show high-ionization emission lines like He II and doubly or triply ionized C and N lines with narrow cores and broad wings, and these emission lines sit atop a smooth blue continuum. The high-ionization level is thought to arise from photoionization of the CSM by a hard radiation field, produced either by a UV/X-ray flash from shock breakout or by the shock when the fastest SN ejecta first crash into the CSM. These high-ionization lines cause the early spectra to resemble Wolf–Rayet (W-R) stars, leading to some claims that this points to W-R progenitors (Gal-Yam et al. 2014). However, the W-R spectral features arise because a slow, dense, H-rich wind is ionized by the SN; the progenitor star is likely to have been cool and potentially even self-obscured by its CSM, and would not have been seen as a W-R star, more likely resembling a cool hypergiant (Groh 2014; Smith et al. 2015). Of course, this would depend on when exactly the progenitor star was observed, since the confined CSM may have just been produced shortly before the SN (i.e., the star may have appeared as a normal RSG or yellow supergiant a few years earlier).

There are several remaining open questions about this class of objects, concerning the mechanism that ionized the CSM (flash from shock breakout or shock interaction), the range of physical properties of the CSM (total CSM mass or mass-loss rate of the progenitor, range of shell and/or envelope radii, asymmetry, composition, etc.), timescale of the mass loss before explosion, details of the evolution of the shock through the CSM, range of initial masses for the progenitors, and so on. All of these help to inform the most important question, which concerns the physical mechanism operating within the star that

caused it to suddenly eject so much mass right before core collapse. The observed velocities of the CSM and the quick disappearance of the narrow lines (and hence, the small inferred outer boundary of the CSM) imply that the strong mass loss occurred very soon before core collapse, perhaps in the last few months or the final year or two of the star’s life. This timescale is a strong hint that something is going haywire in the star during the last rapid phases of nuclear burning (Ne, O, or Si burning), and several ideas have been proposed for extreme mass loss triggered during these phases (Arnett & Meakin 2011; Quataert & Shiode 2012; Shiode et al. 2013; Shiode & Quataert 2014; Smith & Arnett 2014; Woosley & Heger 2015; Fuller 2017; Wu & Fuller 2021). Since the CSM interaction is so short-lived (and the total CSM mass estimates are on the order of $0.1 M_{\odot}$), and as these objects evolve into relatively normal SN types when the narrow lines fade (perhaps implicating moderately massive 10–20 M_{\odot} red or yellow supergiant progenitors), it is unlikely that some other mechanisms proposed for pre-SN mass loss in SNe IIn will be applicable to this particular class. For instance, pulsational-pair instability eruptions (Woosley 2017) are limited to only very high initial masses, and are probably ruled out for these objects. Also, it is difficult to understand why strong pulsationally driven superwinds from very luminous RSGs (Yoon & Cantiello 2010) would only operate for ~ 1 yr before core collapse. In any case, the range of physical parameters for the CSM deduced from studies of individual events can help inform what mechanism ejected the CSM. Perhaps it can also help to understand how or if these objects are connected to the broader class of interacting SNe IIn, or if they are a distinct phenomenon.

Here we discuss a new member of this class, SN 2023ixf, which exploded in the very nearby spiral galaxy M101. It was discovered by K. Itagaki on 2023 May 19, and was soon classified as a Type II SN by Perley et al. (2023). In the following, we adopt a host redshift for M101 of $z = 0.000804$ (de Vaucouleurs et al. 1995). From examining preexplosion archival images, a candidate progenitor consistent with a moderate-luminosity RSG progenitor has been identified (Kilpatrick et al. 2023; Pledger & Shara 2023; Soraisam et al. 2023; Jenson et al. 2023), suggesting a star that had an initial mass of around 12–17 M_{\odot} .

SN 2023ixf was quickly rising at the time of discovery and was expected to become very bright, and because it was a Type II event that could potentially show early narrow lines in the spectra, we chose to initiate an intensive observing campaign to obtain high-resolution echelle spectra every night (or almost every night) for the first week or so after discovery, in order to document rapid changes in the narrow emission from CSM. These observations and initial results are described here, while companion papers describe the early light curve (Hosseinzadeh et al. 2023) and low-resolution spectra (Bostroem et al. 2023). Section 2 describes the observations, Section 3 describes the resulting data and analysis, and Section 4 presents our interpretation of these early data.

2. Observations

Shortly after discovery, we initiated a campaign to obtain observations of SN 2023ixf with a nearly nightly cadence using the Potsdam Echelle Polarimetric and Spectroscopic Instrument (PEPSI; Strassmeier et al. 2018) mounted on the Large Binocular Telescope (LBT) located on Mt. Graham, AZ. PEPSI is a

Table 1
Log of LBT/PEPSI Observations

Date (UTC)	MJD	Epoch (days)	Airmass
2023-05-21	60085.373	2.62	1.35
2023-05-22	60086.244	3.49	1.08
2023-05-23	60087.150	4.40	1.14
2023-05-24	60088.155	5.40	1.12
2023-05-26	60090.357	7.60	1.34
2023-05-27	60091.183	8.43	1.08
2023-06-05	60100.329	17.56	1.34

cross-dispersed echelle spectrograph with separate blue and red channels, each with three wavelength ranges corresponding to three cross dispersers (CDs), with CD I, II, and III in the blue arm, and CD IV, V, and VI in the red arm. When combined, these are designed to cover the full optical wavelength range with no gaps. At the time of these observations, CD I and CD III were not available, so we used CD II (covering 4219–4787 Å) in the blue channel, and CD IV (5361–6316 Å), CD V (6232–7428 Å) and CD VI (7351–9064 Å) in the red channel. All observations were composed of a 60 minutes blue channel exposure with CD II and three 20 minutes red channel exposures with CD IV, CD V, and CD VI. We used a 300 μm fiber (2.2 arcsec diameter) corresponding to a spectral resolving power of $R = \lambda/\Delta\lambda = 50,000$, or a velocity resolution of about 6 km s⁻¹.

The data were reduced using the Spectroscopic Data Systems pipeline (Ilyin 2000; Strassmeier et al. 2018). The pipeline performs bias subtraction and flat field correction, order tracing and optimal extraction with cosmic ray elimination, and wavelength calibration. The spectral orders are normalized in 2D with a nonlinear constrained least-squares fit to account for broad emission lines spanned over adjacent spectral orders. Finally, the spectral orders are rectified into a single spectrum for each CD. The wavelength scale was reduced to the solar system Barycentric rest frame using JPL ephemerides. The pipeline also estimates the variance in each pixel.

Based on early photometry and upper limits, Hosseinzadeh et al. (2023) estimate a likely explosion time of MJD = 60082.75. Using this as a reference, our LBT/PEPSI spectra were obtained between 2 and 9 days after explosion, plus one additional later epoch. We use this date to calculate the time since explosion for each PEPSI spectrum, listed as the third column in Table 1.

3. Results

An example of the resulting normalized PEPSI spectrum of SN 2023ixf is shown in Figure 1. This shows the spectra on days 2.6 (blue), 3.5 (black), and 7.6 (magenta). Although the spectrum appears somewhat complicated, most of the structure results from complex telluric absorption bands, which are labeled in blue in Figure 1. Overall, the spectrum of SN 2023ixf at these early times is dominated by a very smooth blue continuum (although the continuum slope is normalized here) plus a small number of prominent lines labeled in red–orange in Figure 1. At this early epoch within only about a week after explosion, it does not yet show any emission or absorption from very broad features associated with the fast SN ejecta. Besides the interstellar absorption from Na I D, the most interesting features are the strong narrow emission lines in the

spectrum that dramatically change strength and shape with time over only a few days: He II $\lambda 4686$, C IV $\lambda\lambda 5801, 5811$, and H α . The spectra also show weak narrow emission N III $\lambda\lambda 4634, 4641$ and C III $\lambda\lambda 4648, 4650$ seen only in our first epoch, as well as weak emission from N IV $\lambda\lambda 7109, 7123$ and He I $\lambda 5876$, the latter of which grows in strength with time (see Figure 2). We discuss each of these lines in turn, after briefly examining the narrow interstellar absorption.

3.1. Na I D and Interstellar Reddening

Because the line-of-sight Milky Way reddening toward M101 of $E(B - V) = 0.0074$ mag (Schlafly & Finkbeiner 2011) is quite low, and because we are primarily examining line profiles in normalized spectra (where the continuum flux is divided out anyway), we make no reddening correction to our echelle spectra. However, high-resolution echelle spectra afford an opportunity to provide a precise constraint on the equivalent width (EW) of the narrow Na I D interstellar absorption lines arising along the line of sight through the host galaxy.

Figure 2 shows a detail of the region of the spectrum around the Na I D₁ and D₂ resonance doublet, which has been corrected for a redshift of $z = 0.000804$. Each epoch of PEPSI spectra is shown, and the nature of narrow absorption lines in the spectrum is remarkably consistent over the various epochs. The blue boxes in Figure 2 indicate the expected positions of the two Na I lines in M101. Indeed, there are two strong narrow absorption features detected here. These are seen to be mixed amid a large number of other weaker narrow absorption features, which may arise from various clouds along the line of sight through the Milky Way at various rotation velocities and a cluster of telluric water absorption lines. This suggests that high spectral resolution is important to accurately estimate the reddening within M101, because its low redshift means that its interstellar absorption features may overlap with those from the Milky Way and these telluric features.

We measure Na I EW values of 0.156 Å for D₁ and 0.187 Å for D₂. The measured EWs were consistent to better than 1% from one epoch to the next; the main uncertainty in the absolute measurement of the EW values is the choice of continuum level, and how much contamination there might be from overlapping lines. Although there are many other weak narrow lines, the continuum level in these spectra is well determined to about 1% of the flux level as well. Following the relations from Poznanski et al. (2012), these EWs translate to a reddening value of $E(B - V) = 0.036$ mag. Following Poznanski et al. (2012), we multiply this by 0.86 to account for the conversion to Schlafly & Finkbeiner (2011) values, yielding a host reddening along the line of sight to SN 2023ixf of $E(B - V) = 0.031$ mag. The uncertainty in the relation from Poznanski et al. (2012) is 30%–40%, which is much larger than any error in $E(B - V)$ introduced by the measurement error in these PEPSI spectra. This resulting value of $E(B - V) = 0.031$ mag is larger than the Milky Way reddening, indicating that the local host dust in M101 is the dominant source of extinction along the line of sight. This may, of course, vastly underestimate the extinction toward the progenitor star arising from dust that may have been present in the pre-SN CSM.

The velocities of these deep Na I D absorption features are also useful later in our analysis, especially when interpreting the velocities of narrow emission components. We measure the centroid velocity of the strongest components of the D₁ and D₂

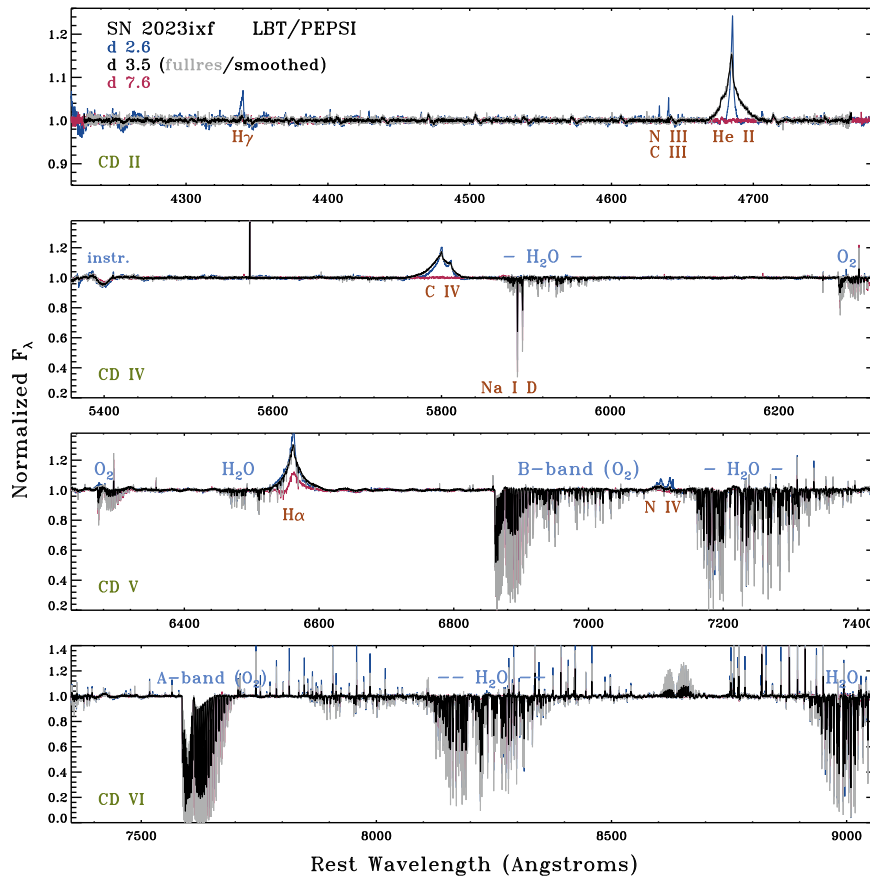


Figure 1. An example of the full wavelength coverage of the PEPSI spectra, showing the first epoch on day 2.6 in blue, the second epoch on day 3.5 in gray (original resolution), and black (smoothed). The spectrum a few days later on day 7.6 is shown in magenta, when the narrow features besides $H\alpha$ have faded. Telluric absorption bands or instrumental features are labeled in blue, lines intrinsic to the SN (or host galaxy) are labeled in red–orange, and the PEPSI cross disperser (CD) is noted in green in the lower left of each panel. Each of the four wavelength ranges shown here results from stitching together several orders, sometimes producing small wiggles in the continuum at locations where edges of orders are joined. This is especially noticeable in CD II with a pattern of wiggles every ~ 30 Å. One of these is on the blue wing of He II $\lambda 4686$. The dip in flux at 5400 Å is a known instrumental artifact of PEPSI.

lines. After correcting the spectra for the adopted host redshift of $z = 0.000804$, we take the average of the two lines to derive a Doppler velocity for the Na I D absorption of $+7$ (± 1) km s^{-1} , relative to the adopted redshift of M101 (which is about $+241$ km s^{-1}). When we interpret the observed velocities below in Section 4, we take this value of $+7$ km s^{-1} as representative of the velocity of interstellar material in the vicinity of SN 2023ixf that results from galactic rotation, and therefore as a likely indication of the progenitor star’s systemic velocity. In figures in this manuscript showing the observed line profiles, the velocity scale is only corrected for $z = 0.000804$, but we show this $+7$ km s^{-1} systemic velocity with a vertical green dashed line.

3.2. High-ionization Features

Notable high-ionization lines in these early time echelle spectra are He II $\lambda 4686$, C IV $\lambda\lambda 5801, 5811$, and N IV $\lambda\lambda 7109, 7123$. The line profile evolution of each of these can be seen in Figures 3(a), (b), and (d), respectively (panel 3(c) shows He I $\lambda 5876$, discussed in the next section). If we take into account the fact that C IV and N IV are closely spaced doublets or blends, the evolution of strength and line profile shape in each of these is similar. All three have relatively strong, narrow ($\lesssim 100$ km s^{-1}), blueshifted (-50 to -150 km s^{-1}) emission peaks with broader wings at the first

epoch. These lines then appear to broaden and fade over the next 2–3 days, and completely disappear 3–4 days later. The evolution of the EWs of these emission lines measured in our PEPSI spectra is shown in Figure 4. All the high-ionization lines fade by factors of 10–20 or more over a time period of 4 days.

The change in width of He II over only 1 day from May 21 to 22 is particularly stunning, where the broad ± 1000 km s^{-1} emission wings come and go very quickly. The He II profile on day 2.6 is narrow, lacking the broad electron scattering wings seen in $H\alpha$ on that same date (as we show below, when we subtract off a 1000 km s^{-1} Lorentzian profile from $H\alpha$, the two line profiles are very similar).⁵ He II then fades and disappears by day 5.4. Of these high-ionization lines, C IV $\lambda\lambda 5801, 5811$ has the broadest wings (extending to -2000 km s^{-1} on the blue side), and it lingers the longest before fading, disappearing from the spectrum about a day later than He II. In any case, all the narrow and intermediate-width emission from these high-ionization features is completely absent from the spectrum by

⁵ We note that some lower-resolution spectra of SN 2023ixf do show broader wings of He II $\lambda 4686$ at very early epochs comparable to our observations (Jacobson-Galan et al. 2023). Because PEPSI spectra are cross-dispersed, the “continuum” level that is normalized in the pipeline reduction may include some of the broadest emission wings if it stretches across more than one order. We find this to be likely, so we caution the reader about the absence of broad He II emission in these spectra, and we do not emphasize this result in our discussion.

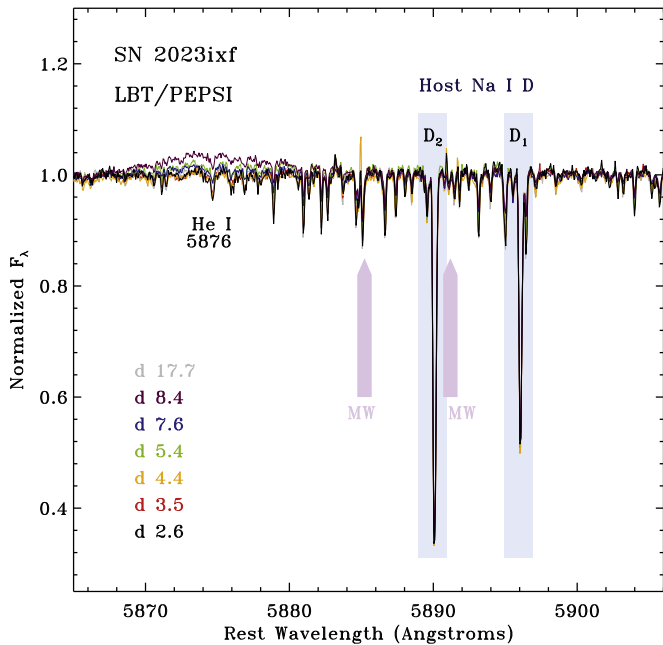


Figure 2. Detail of the region around the Na I D interstellar absorption doublet seen toward SN 2023ixf in PEPSI spectra. The light blue boxes show the expected locations of the Na I lines for the host, and the lavender pointed boxes show the Na I line locations for zero redshift, appropriate for features in the Milky Way (blueshifted here because the spectra have been corrected for the redshift of M101). Changes in intermediate-width emission from He I $\lambda 5876$ are also visible, and are discussed in more detail in Section 3.2.

day 7.6. The narrow emission component fades more quickly, leaving only a fainter intermediate-width component to persist for a few days. High-ionization emission might fade either because the gas cools and recombines, or because the CSM is overtaken by the SN; we return to this topic later in Section 4.

There is a persistent weak emission feature on the blue wing of He II at about -450 km s^{-1} , possibly with a P Cygni profile. This is most likely an artifact that arises where edges of echelle orders are merged (see the top panel of Figure 1, as noted earlier). This is probably not emission from N III $\lambda\lambda 4679.4, 4679.8$, which is, however, seen in low-resolution spectra a day earlier (Bostroem et al. 2023).

Notable for their general absence in our PEPSI spectra are N III $\lambda\lambda 4634, 4641$ and C III $\lambda\lambda 4648, 4650$. Together with He II $\lambda 4686$, these lines constitute the so-called blue W-R bump. In many examples of SNe II with fleeting CSM interaction signatures, these N III/C III lines are very strong (often equal in strength to He II $\lambda 4686$), and with strong electron scattering wings (Niemela et al. 1985; Leonard et al. 2000; Gal-Yam et al. 2014; Smith et al. 2015; Jacobson-Galán et al. 2022; Terreran et al. 2022). In fact, these N III/C III lines are seen in our spectra of SN 2023ixf, but only in our first spectrum on day 2.6, where they are extremely weak (Figure 5). For N III $\lambda\lambda 4634, 4641$ we measure EWs of 0.022 ± 0.004 and $0.035 \pm 0.005 \text{ \AA}$, respectively, and for C III $\lambda\lambda 4648, 4650$, we measure EWs of 0.013 ± 0.003 and $0.008 \pm 0.002 \text{ \AA}$, respectively. The lines disappear the next day. Also, when seen on day 2.6, they only show the narrow emission components with no broad wings; these narrow components have the same blueshift and approximately the same width as He II (Figure 5). These lines are stronger the previous day in lower-resolution spectra (Bostroem et al. 2023), as noted above for N III $\lambda\lambda 4679.4, 4679.8$. Over the same period from day 2.6 to 3.5

when these lines vanish from our spectra, the strengths of C IV and He II are still increasing (Figure 4). This indicates that, even as late as 2–3 days after explosion, the compact CSM is still increasing in ionization level, even though the light travel time to 20–30 au is only about 3 hr. This suggests that a sudden flash of ionization from shock breakout is probably not the primary ionization source for the CSM, which may instead be photoionized by emission from the ongoing CSM interaction shock (Smith et al. 2015; Terreran et al. 2022).

3.3. Recombination of He II to He I

The detailed evolution of He I $\lambda 5876$ is shown in Figure 3(c). This line is often seen as a strong narrow emission line in early SNe II with CSM signatures, and in SNe IIn, but it is totally absent in the first two epochs of our echelle spectra of SN 2023ixf. Interestingly, however, He I $\lambda 5876$ starts to grow in strength and becomes an admittedly still very weak intermediate-width emission feature by days 7.6 and 8.4 (blue and violet in Figure 3(c); note that this line is found amid a forest of telluric H_2O absorption features). Figure 4 shows the EWs of He I emission as compared to other lines, demonstrating how the strength of He I emission increases as He II and the other high-ionization lines fade away over 4–5 days. (Note that while the actual value of the EW for He I is quite uncertain because of all the overlapping telluric absorption, the relative increase in strength of He I shown in Figure 4 is real because the forest of telluric lines does not alter the flux passing between them.) The line profiles of He I during this evolution can be seen in Figure 2 as noted earlier, but are shown more clearly in Figure 3(c). The emission component of He I has a width of about $500\text{--}1000 \text{ km s}^{-1}$; there is no narrow emission from He I $\lambda 5876$ that would correspond to the blueshifted, narrow ($50\text{--}100 \text{ km s}^{-1}$) peak of He II in the first epoch. He I $\lambda 5876$ shows weaker intermediate-width P Cyg absorption, discussed more below.

This lack of narrow emission indicates that the weak He I $\lambda 5876$ emission detected in these spectra is arising from accelerated gas that has already been swept up by the shock and is now cooling and recombining. Accordingly, this indicates that the narrow component of He II (and by extension, the narrow components of N IV and C IV) disappears because the slow gas is accelerated by the shock, not because it survives as pre-shock CSM and recombines.

Figure 6 compares profiles of the fading He II $\lambda 4686$ emission to the last epoch of He I $\lambda 5876$ emission. Note that, as He II $\lambda 4686$ emission wings within $\pm 1000 \text{ km s}^{-1}$ fade away, the He I $\lambda 5876$ emission and P Cygni absorption over the same range of velocities become stronger. This suggests that the gas expanding at around 1000 km s^{-1} is cooling and recombining. These velocities are significantly faster than the narrow ($50\text{--}100 \text{ km s}^{-1}$) component from the unshocked CSM seen in the first-epoch spectra. Again, this confirms that the He I-emitting gas has been accelerated, probably because it is now in the post-shock shell of swept-up CSM. The He I $\lambda 5876$ profile on day 8.4 also shows a weak and broad P Cygni absorption feature at -500 to -1200 km s^{-1} , which is similar to the later epochs of He I discussed below.

Interestingly, we do not see a similar ionization transition in alpha elements. While C IV and N IV fade quickly over a few days, we do not see a corresponding growth in the strength of N III or C III lines that are seen in several other SNe II with early narrow CSM features, as noted above. At the end of our

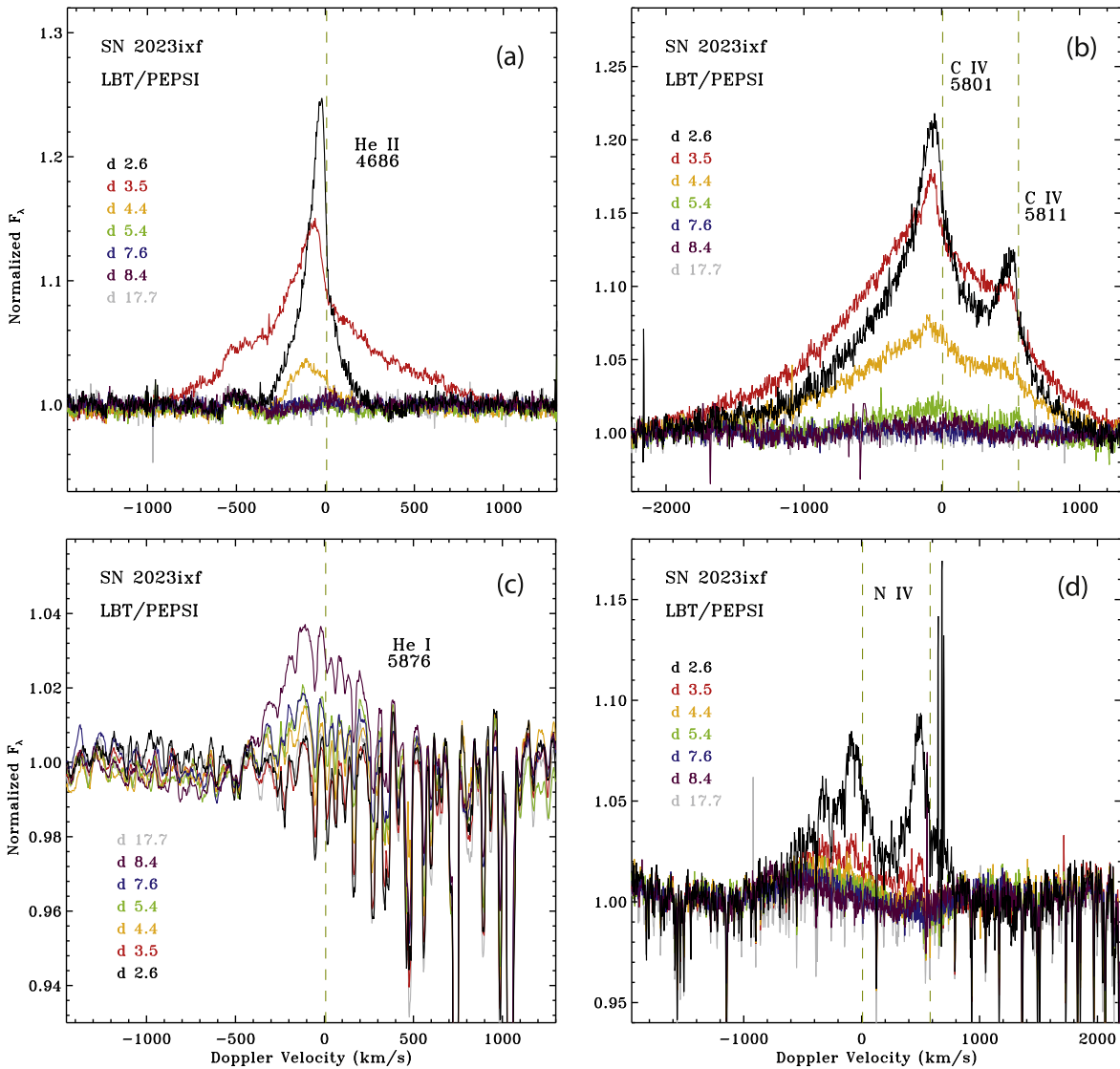


Figure 3. Evolution of individual line profiles for (a) He II $\lambda 4686$, (b) the C IV $\lambda\lambda 5801, 5811$ doublet (velocity scale set for $\lambda 5801$), (c) He I $\lambda 5876$, and (d) the N IV $\lambda\lambda 7109, 7123$ doublet (velocity scale set for $\lambda 7123$). Spectra have been corrected for the redshift of M101, $z = 0.000804$, and for each line, velocity = $+7 \text{ km s}^{-1}$ (the presumed systemic velocity) is shown by a vertical green dashed line (see text). Note that for the day 8.4 spectrum of C IV (panel (b)) there was no line flux detected, but there were a few noise spikes or hot pixels in the spectrum that we clipped at a normalized flux level of 1.02 for clarity in this figure.

spectral series, the C III and N III emission features do not turn on as the C IV and N IV fade. This implies that the C IV and N IV are not fading primarily because the N and C ions are recombining to a lower-ionization state. Instead, it may suggest that the CSM and shocked shell are largely getting enveloped by the expanding SN photosphere after a week; this is discussed more below.

3.4. Intermediate-width and Narrow $H\alpha$

$H\alpha$ exhibits the most interesting and informative evolution of the lines seen in the spectrum during the first week after explosion (Figure 7). Overall, $H\alpha$ displays a clear and steady evolution from a narrow line core with broad Lorentzian-shaped wings at the first epoch, transitioning to a clear intermediate-width P Cygni profile a week later. It is similar to the evolution seen in normal SNe II_n, but on a vastly compressed timescale. The narrow component fades more rapidly than the intermediate-width component. Overall, the

EW of $H\alpha$ fades by about a factor of 5 in the first week (Figure 4), during a time when the r magnitude only brightens modestly (Hosseinzadeh et al. 2023), corresponding to a factor of ~ 1.6 increase in continuum flux. This indicates that the narrow and intermediate $H\alpha$ line luminosity fades by a factor of ~ 3 during the first week of observations. By 2 weeks after explosion (day 17.7 in Figure 7), the intermediate-width emission component of $H\alpha$ is gone. Some of the details of the line profile evolution are interesting. Note that $H\alpha$ is blended with weak emission from He II $\lambda 6560$, which produces a small bump of excess emission on the blue wing of $H\alpha$ at -130 km s^{-1} ; this is discussed at the end of the current section.

First, we consider the evolution of the intermediate-width component. Aside from an overall fading with time, the shape of the red wing of the line changes little, with a gradual reduction in maximum velocity from about $+2000 \text{ km s}^{-1}$ on the first epoch down to about $+1000 \text{ km s}^{-1}$ a week later. Some of this apparent slowing may simply arise because the

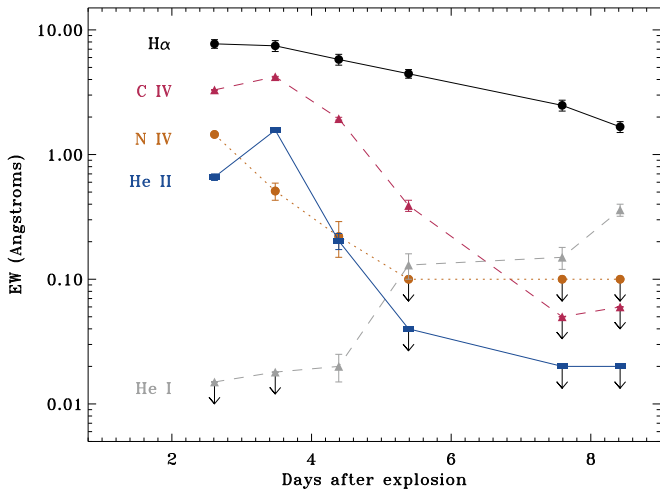


Figure 4. Measured equivalent widths (EW; emission lines have positive values here) for $H\alpha$, $He\ II\ \lambda 4686$, $C\ IV\ \lambda\lambda 5801, 5811$, $He\ I\ \lambda 5876$, and $N\ IV\ \lambda\lambda 7109, 7123$. The EW here is the integrated flux of the line (not a functional fit) divided by the continuum level, and the EW error bars are dominated by the noise in the nearby continuum level for these lines.

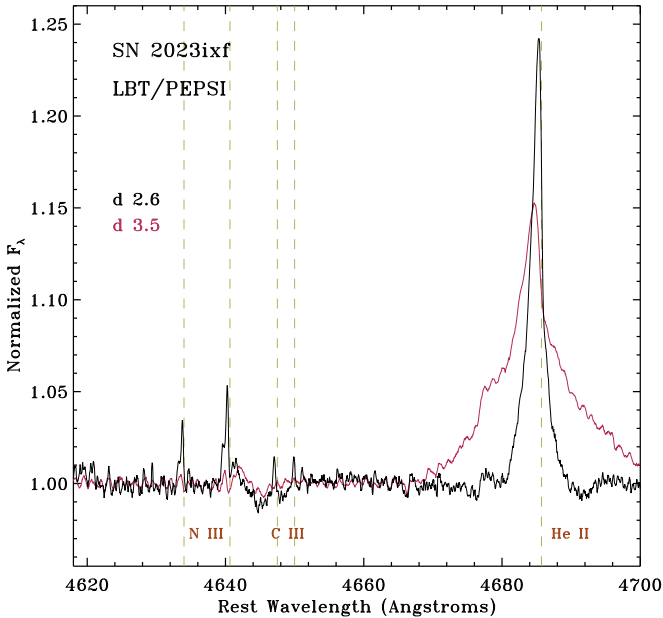


Figure 5. A detail of the spectrum in the wavelength range of the blue W-R bump, including $He\ II\ \lambda 4686$, as well as the $N\ III\ \lambda\lambda 4634, 4641$ and $C\ III\ \lambda\lambda 4648, 4650$ lines. For each line, the $+7\ km\ s^{-1}$ systemic velocity is marked by a vertical dashed green line. The $N\ III$ and $C\ III$ lines are only detected on our first epoch on day 2.6 where they appear weak, narrow, and blueshifted.

extremes of the line wings fade below the noise, but it may also result from cooling of the region where the electron scattering occurs.

There are more dramatic and important changes occurring on the blue wing of the line. At first, the blue wing appears as a nearly symmetric reflection of the red wing, extending to $-2000\ km\ s^{-1}$. However, the blue side fades more quickly than the red wing, steadily transforming into an intermediate-width P Cygni absorption feature with a trough at $-700\ km\ s^{-1}$ and a blue edge at about $-1300\ km\ s^{-1}$. This change is physically significant. The intermediate-width wings of interacting SNe are often presumed to be caused by thermal electron scattering of the narrow line emission, broadening those narrow line

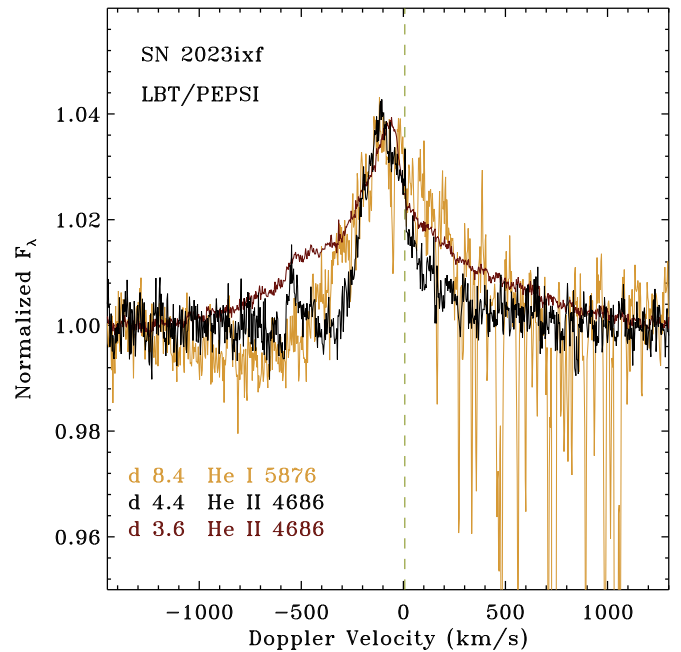


Figure 6. The line profile shape of the fading $He\ II\ \lambda 4686$ emission on days 3.6 (red) and 4.4 (black), as compared to the $He\ I\ \lambda 5876$ emission a few days later (orange). As $He\ II\ \lambda 4686$ emission wings within $\pm 1000\ km\ s^{-1}$ fade, $He\ I\ \lambda 5876$ emission and P Cygni absorption over the same range of wavelengths become stronger. This suggests that the gas expanding at around $1000\ km\ s^{-1}$ (i.e., gas in the post-shock shell of swept-up CSM) is cooling and recombining.

photons into wings that can be approximated by a Lorentzian shape (Chugai 2001; Smith et al. 2008; Smith 2017). This is the case for our first spectrum on day 2.6 (Figure 8). A Lorentzian with an $FWHM = 1000\ km\ s^{-1}$ and with a center shifted $105\ km\ s^{-1}$ to the blue matches the line shapes of $H\alpha$ on day 2.6 reasonably well, except for some low-level broad excess emission on the blue wing. Electron scattering is thermal, and the wings are expected to be symmetric about the wavelength of the original narrow-line photons.⁶ Therefore, the $-105\ km\ s^{-1}$ blueshifted centroid of this $1000\ km\ s^{-1}$ Lorentzian makes sense in this case, since the narrow emission that is being scattered and broadened spans a similar range of velocity.

However, electron scattering cannot turn narrow emission into a broad absorption feature. The transition of SN 2023ixf’s $H\alpha$ line to an intermediate-width P Cygni absorption feature requires that after day 3, we are seeing Doppler-shifted absorption and emission by accelerated H atoms in the post-shock gas, and not emission from slow-moving pre-shock gas that has been broadened mostly by electron scattering (although electron scattering may obviously still influence the red wing of the line, for example).

The fact that this broader absorption increases in strength over a time period when the narrow emission component mostly fades away strongly suggests that after a few days, most of the pre-shock CSM has been swept up by the shock. After

⁶ Though, note that the original velocity of the line photons that were scattered and therefore define the center of the Lorentzian (at $-105\ km\ s^{-1}$) is not necessarily the same as the velocity of the observed narrow line photons that have escaped without scattering ($-22\ km\ s^{-1}$) if there is asymmetry, asymmetric illumination of the CSM, or a velocity gradient in the CSM; this is likely to be the case, as we discuss later in Section 4. However, the observed narrow emission does span a range of velocity that includes the centroid of the Lorentzian.

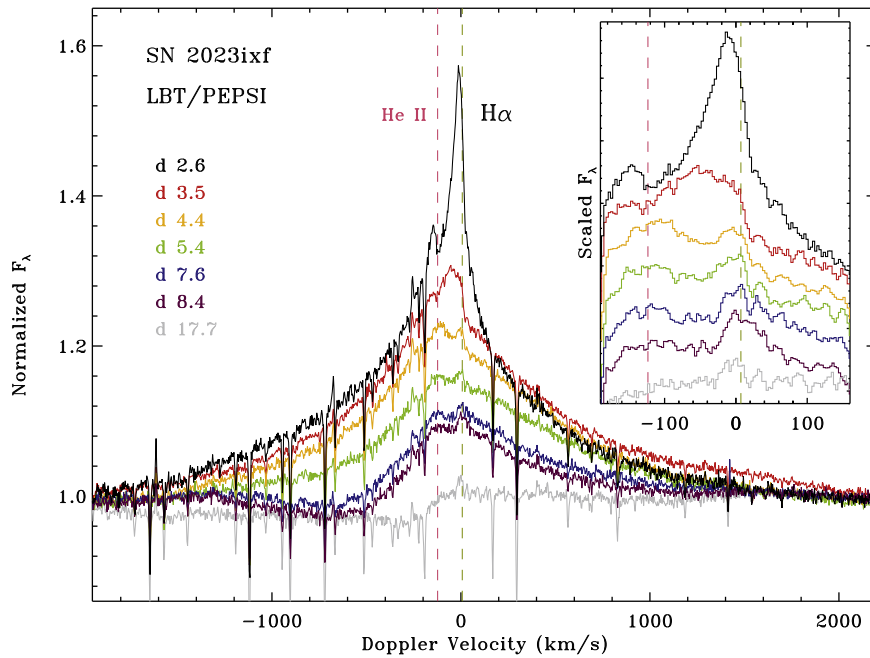


Figure 7. Same as Figure 3, but for the $H\alpha$ line profile. The inset in the upper right zooms-in on the narrow component. Note that the emission bump at around -130 km s^{-1} is not a velocity component of $H\alpha$, but is instead emission from the weaker He II $\lambda 6560$ line that overlaps (its $+7$ km s^{-1} systemic velocity is marked with a magenta vertical dashed line). In this case, it would therefore be incorrect to interpret the drop in flux between this feature and the narrow $H\alpha$ emission peak as narrow P Cygni absorption of $H\alpha$.

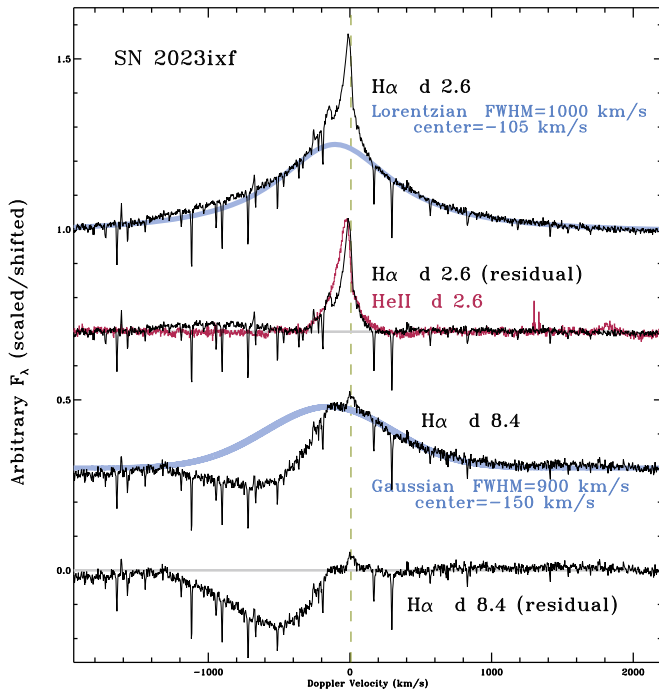


Figure 8. Details of the $H\alpha$ profile. The top spectrum is the $H\alpha$ profile observed on our first epoch on day 2.6, compared to a Lorentzian function with $\text{FWHM} = 1000$ km s^{-1} and a centroid shifted to the blue by 105 km s^{-1} . This gives an adequate match to the red wing, but not the central peak or blue wing. The residual after subtracting this Lorentzian curve is shown in the second tracing from the top (black), which is then compared to the observed He II $\lambda 6560$ profile on the same date (plotted in magenta). The third spectrum down shows the observed $H\alpha$ profile on day 8.4 compared to a Gaussian with $\text{FWHM} = 900$ km s^{-1} that has its centroid shifted 150 km s^{-1} to the blue. Finally, the bottom tracing shows the residual after subtracting this Gaussian, highlighting the shape of the blueshifted absorption feature.

that, $H\alpha$ emission and absorption trace CSM that has been hit by the forward shock and accelerated, being swept up into a dense post-shock shell (often called the *cold dense shell*, or CDS, in SNe II). By day 8.4, the red wing of the line can no longer be well matched by a Lorentzian shape; instead, a Gaussian function with $\text{FWHM} = 900$ km s^{-1} and with its center shifted to the blue by 150 km s^{-1} gives a better match (Figure 8). The fact that the CDS is seen in absorption against the SN continuum photosphere requires that it has indeed cooled. Similar intermediate-width absorption features arising in the CDS are seen in some SNe II, including SN 2006gy (Smith et al. 2010) and SN 1994W (Chugai et al. 2004). We also note that the width and shape of the $H\alpha$ P Cygni profile on day 8.4 are very similar to those of He I $\lambda 5876$ on the same date (Figure 6).

Although the intermediate-width $H\alpha$ persists longer than the high-ionization lines, it does not last long. Figure 7 also shows the observed $H\alpha$ profile in a PEPSI spectrum on day 17.6 (gray). While there is a gap in our spectral coverage, this shows that the intermediate-width emission component of $H\alpha$ is gone by a little over 2 weeks after explosion. There is still a kink at around zero velocity, hinting at some persistent intermediate-width P Cygni absorption of $H\alpha$ at this time. However, there is also a deficit of flux at high velocity (resembling a lower continuum level on the blueshifted side of the line on day 17.6; Figure 7), suggesting that the broad absorption from SN ejecta is beginning to influence the spectra by this epoch.

The narrow component of $H\alpha$, presumably arising from the pre-shock CSM, shows surprisingly complex profile evolution. Excluding the effects of broadening from electron scattering discussed above, one might expect to see a very narrow (10 – 20 km s^{-1}) and symmetric profile shape from the core of

an emission line arising from a more-or-less spherical and slow RSG wind, but this is evidently not the case in SN 2023ixf.

The inset (upper right) in Figure 7 documents changes in line profile shape of the narrow component of $H\alpha$ (see also Figure 8). At our first epoch (day 2.6; black), the narrow component is asymmetric (a broader blue wing and sharper drop on the red side), it has a blueshifted centroid (at about -25 km s^{-1}), and it has an FWHM of 48 km s^{-1} . At the second epoch on day 3.5 (red), it becomes weaker, broader (FWHM = 79 km s^{-1}), and even more blueshifted (centroid velocity of -42 km s^{-1}). In both of these first two epochs, the narrow component seems rather abruptly cut off at zero velocity on the red wing. After that, the narrow component becomes much weaker, and settles down to a more symmetric and narrower (FWHM $\approx 45 \text{ km s}^{-1}$) emission component that has a centroid closer to zero velocity or even slightly redshifted (about $+8 \text{ km s}^{-1}$). At all epochs, the FWHM of the narrow component is resolved, being significantly larger than the instrumental resolution of about 6 km s^{-1} .

How shall we interpret the changing offsets in the centroid velocities of the narrow emission component? In Section 3.1, we noted that the centroid velocities of the interstellar Na I D absorption (after correction for M101's redshift of $z = 0.000804$) were $+7 \text{ km s}^{-1}$, which we take to be the likely systemic velocity of the progenitor. This agrees (to within 1 km s^{-1}) with the centroid velocity that we measure for the narrow $H\alpha$ component at ~ 1 week post-explosion. One possible interpretation of this is that the lingering narrow emission centered on the systemic velocity with a resolved width of 45 km s^{-1} corresponds to the photoionized gas in distant regions of the progenitor's RSG wind, which may be roughly spherical, or at least symmetric about the systemic velocity. This, in turn, means that the pronounced blueshift of the narrow $H\alpha$ component on days 2–3 (as well as the similar blueshift of narrow components of He II and other high-ionization lines on these same dates) is real. Thus, in early epochs, we are seeing emission from inner regions of the CSM that are predominantly on the near side of the SN, which are expanding toward us at $30\text{--}50 \text{ km s}^{-1}$ or more (the observed blueshifts are even larger for higher-ionization lines). We return to the implications of this blueshifted narrow emission later in Section 4.

At no time during the first week do the spectra show any hint of a narrow P Cygni absorption component in $H\alpha$ that might arise from absorption along the line of sight through dense, slow, pre-shock CSM. Such narrow absorption features from the pre-shock CSM are often seen in SNe IIn, providing that spectra have sufficient resolution (e.g., Salamanca et al. 2002; Trundle et al. 2008; Smith et al. 2010; Chugai 2019; Smith & Andrews 2020). We note that the narrow emission bump seen at -130 km s^{-1} is actually weak narrow emission from He II $\lambda 6560$ superposed on the blue side of the $H\alpha$ line. It is not a separate velocity component of $H\alpha$, and the gap between these two is not narrow P Cygni absorption of $H\alpha$. The expected systemic velocity of this He II line is marked with a vertical dashed magenta line in Figure 7. The emission feature in question is blueshifted from this reference position by about -30 km s^{-1} , similar to the blueshift of the narrow components in other lines at the same early epoch. The lack of narrow P Cyg absorption may suggest that the CSM is asymmetric, as discussed below.

4. Discussion

4.1. Blueshifted Narrow Features and the CSM Speed

As noted above, all of the emission lines seen in our first PEPSI epoch on day 2.6 have narrow emission peaks that are blueshifted (see Figures 3 and 7). Recall that the presumed systemic velocity of SN 2023ixf (indicated by Na I D absorption) is at $+7 \text{ km s}^{-1}$ relative to the average redshift of M101. Relative to the systemic velocity, the narrow $H\alpha$ peak is at -22 km s^{-1} , and the narrow emission component extends from about $+15 \text{ km s}^{-1}$ at the drop on the red side, reaching out to about -100 km s^{-1} or more on the blue side. Similarly, the high-ionization lines (He II, C IV, N IV) have their strongest narrow emission on day 2.6 ranging from about 0 to -150 or -200 km s^{-1} .

Thus, it appears that the narrow emission on day 2.6 is being emitted by expanding CSM that is primarily on the near (approaching) side of the SN. This has been seen before in early spectra of interacting SNe, and seems to be well understood as being due to the combined effects of light travel time in the presence of a variable illumination source and occultation by the SN photosphere (Groh 2014; Shivvers et al. 2015; Gräfener & Vink 2016). This does not mean that the CSM is actually one sided, but that we are not able to detect as much emission from the redshifted side of the CSM because it is blocked from our view or not yet fully illuminated, depending on the time after explosion. If much of the redshifted CSM emission is missing, this is important for interpreting the velocities.

Figure 9 shows a detail of the narrow $H\alpha$ component in our first spectrum, after subtracting away a broad Lorentzian as in Figure 8. This is compared to a narrow Lorentzian function centered at the systemic velocity of $+7 \text{ km s}^{-1}$, matching the blue wing of $H\alpha$ (note that this curve does not match the excess emission bump at -130 km s^{-1} , which is due to emission from He II $\lambda 6560$ superposed on the $H\alpha$ line; with this assumed line center at $+7 \text{ km s}^{-1}$, the uncertainty in the Lorentzian FWHM is about $\pm 10 \text{ km s}^{-1}$). This symmetric Lorentzian curve demonstrates what the true symmetric narrow $H\alpha$ emission from the CSM would look like at this epoch, if we could detect all of it. This, in turn, tells us that the CSM expansion speed indicated by the narrow $H\alpha$ profile is actually about 115 km s^{-1} . This is much faster than a typical RSG wind of $\sim 20 \text{ km s}^{-1}$.

However, interpreting this blueshifted emission is complicated by the fact that the amount of blueshift is different for different lines (tracing different ionization levels), and the amount of blueshift in the narrow components is time dependent. This is discussed next.

4.2. Acceleration of the Pre-shock CSM

Figure 9 illustrates the complex time-dependent and ionization-dependent evolution of the narrow emission components from the pre-shock CSM in our first two epochs of PEPSI spectra (these are days 2.6 and 3.5, shown in the middle and bottom tracings in Figure 9, respectively). Note that we have removed the broader wings of these profiles by subtracting Lorentzian functions with FWHM values of around 1000 km s^{-1} (as shown for $H\alpha$ in Figure 8). Figure 9 includes the narrow profiles of $H\alpha$ (black), He II (magenta), and C IV (green), which trace recombination emission from increasing ionization levels (13.6, 54.4, and 64.5 eV, respectively).

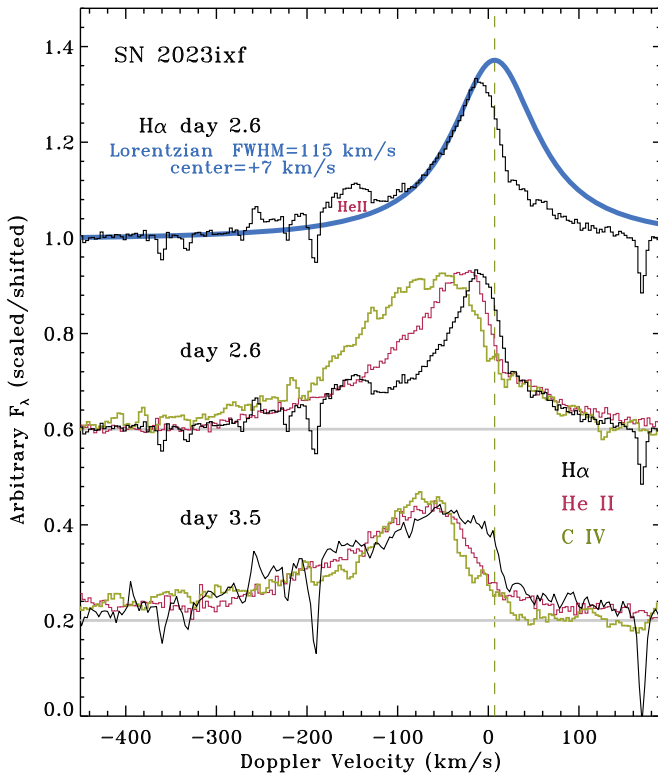


Figure 9. Details of the narrow-line profiles in our first two epochs of PEPSI spectra. The top spectrum here is the same as the second spectrum from the top shown in Figure 8. This is the narrow $H\alpha$ profile on day 2.6, which is the residual flux remaining after subtracting away a broad Lorentzian with $\text{FWHM} = 1000 \text{ km s}^{-1}$. For comparison, a symmetric narrow Lorentzian function with $\text{FWHM} = 115 \text{ km s}^{-1}$ is shown in blue, centered at the systemic velocity of $+7 \text{ km s}^{-1}$ (indicated by the green vertical dashed line). This Lorentzian function matches the blue wing of the line, and is meant to illustrate what the full intrinsic symmetric narrow $H\alpha$ emission profile from the CSM would look like if the red side of the line were not missing. Recall that the bump at -130 km s^{-1} is $\text{He II } \lambda 6560$. The bottom two plots show tracings of the narrow components of $H\alpha$ (black), $\text{He II } \lambda 4686$ (magenta), and $\text{C IV } \lambda 5801$ (green) overplotted, on day 2.6 (middle) and day 3.5 (bottom). As with the top plot, each of these has had a broad Lorentzian subtracted in order to highlight the narrow emission.

Figure 9 does not include N IV because of its relatively low signal-to-noise.

On day 2.6 (middle tracings), all the narrow lines are blueshifted, but there is a remarkable and systematic increase in both width and in the amount of blueshift of the line center as we move from $H\alpha$ to He II and then to C IV . Basically, higher-ionization lines exhibit faster outflow speed. There are two potential explanations for this.

1. The source function for each of these lines may have a slightly different radial dependence in an ionized pre-shock CSM, because of radial gradients in CSM density and ionization level (e.g., Groh 2014). For example, one might expect higher-ionization lines to arise closer the shock, and $H\alpha$ to be emitted from a more distant region. If there is a velocity gradient in the CSM (with faster velocities at smaller radii), this might account for why higher-ionization lines show faster outflow speeds. However, this would require a very steep velocity gradient (increasing by a factor of more than 2 from $H\alpha$ to C IV) in a narrow radial zone. In the models presented by Groh (2014), the CSM velocity was assumed to be constant with radius, but new models

may be able to quantify the velocity gradient that would be needed to explain the observed profiles. The required velocity gradient not only is steep but decreases with radius (faster outflow at smaller radii). This is the opposite of what is expected for a Hubble-like flow from a sudden burst of pre-SN mass loss, and it is the opposite of an acceleration zone of a stellar wind that eventually reaches its terminal speed at a large radius. Instead, it would point either to the dramatic radiative acceleration of the inner pre-shock CSM by the radiation from the shock itself or to an outflow speed that was increasing during the few years preceding explosion. If the CSM is very dense, a small mean free path could lead to a sharp velocity gradient immediately ahead of the shock, and this would be an interesting problem for detailed models to quantify. On the other hand, a rapidly changing outflow speed in the pre-SN ejection is perhaps plausible but is ad hoc.

2. Another possibility is that the CSM is asymmetric. Imagine that the SN blast wave hits CSM with a disk or torus geometry that has a dropping density away from the equatorial plane. In the equatorial plane, the forward shock will hit the densest CSM and will be decelerated the most. Moving out of the plane, the shock will encounter relatively less dense CSM, and hence, the forward shock will decelerate less and will continue outward at a higher speed. At these intermediate latitudes, the faster shock will yield hotter post-shock gas, and so the CSM immediately ahead of the shock will be illuminated by a harder radiation field from the shock. Thus, we might expect to see higher-ionization tracers (i.e., C IV) coming preferentially from higher latitudes in the immediate pre-shock environment, and lower ionization ($H\alpha$) emitted by CSM in the dense equatorial plane. The different velocities at the different ionization might then arise because the less dense CSM out of the plane also has less inertia, and will therefore experience more radiative acceleration, or because the gas at mid-latitudes was ejected with higher speeds than the gas in the equator, as commonly seen in bipolar nebulae. This is a difficult scenario to investigate theoretically, because it requires 3D radiation hydrodynamics with a line transfer. However, if the pre-shock mean free path is small at these high densities, one might address the question with a series of spherical calculations with shocks running into a range of different CSM density.

So far, we have only discussed the narrow profiles in our first epoch on day 2.6; the bottom tracings in Figure 9 show that the situation changes markedly 1 day later on day 3.5. Namely, the stark differences in velocity in the three different lines are mostly gone. While the red edge of the narrow component of $H\alpha$ still extends closer to zero, the width and blueshifted centroid velocity are now much more similar for the three lines. The essential change is that most of the narrow peak of $H\alpha$ is gone, making the $H\alpha$ line appear broader and more blueshifted (see the inset of Figure 7), and He II has changed in a similar fashion although to a lesser degree, making all three lines similar. The factor of 2 difference in velocity between $H\alpha$ and C IV is now gone. As above, there are again two potential explanations for this change:

1. We may be seeing direct evidence for the pre-shock radiative acceleration of CSM. After more time has passed, the radiation field has accelerated the rest of the slower CSM traced by $H\alpha$ emission so that it now shares the faster expansion speeds seen in higher-ionization gas. Detailed models would be needed to confirm that the timescale and amount of acceleration (as well as the difference between $H\alpha$ and the higher-ionization lines) are plausible.
2. Another possibility arises if the CSM is asymmetric. As noted earlier, the slowest and densest CSM in the equatorial plane that emitted the narrow peak of $H\alpha$ would be at a smaller radius because the blast wave in this direction gets decelerated the most. As such, the dense and slow equatorial CSM at the narrow pinched waist would be the first to be enveloped by the expanding SN photosphere. In this scenario, the $H\alpha$ line would appear broader simply because the narrowest emission is engulfed and hidden by the SN ejecta and therefore removed from the observed line profile, not because that slow gas is accelerated. This would be consistent with the fact that the flux of the narrow component of $H\alpha$ drops precipitously in this first day, and with the apparent change in shape of the narrow $H\alpha$ line (again, see the day 2.6 and day 3.5 profiles in the inset of Figure 7).

One difference that may help discriminate between these two possibilities concerns the relative density of the emitting CSM. In the spherical case (the first option for both epochs is discussed above), the narrower $H\alpha$ emission comes from lower-ionization zones at larger radii, and therefore should have lower densities compared to the He II and C IV emitting zones. In the aspherical second case, the narrowest $H\alpha$ is emitted by the densest CSM at the equator, while the higher speeds at higher ionization result from lower densities at higher latitudes. Perhaps future modeling of the spectrum can help quantify the physical conditions in the emitting zones. Although it is tempting to ascribe the increasing $H\alpha$ speed from day 2.6 to day 3.5 to radiative acceleration of the CSM, it is difficult to confirm this with available information because asymmetry (which might be expected anyway) also provides a suitable and perhaps more straightforward explanation.

4.3. Disappearing Narrow Lines and CSM Radius

Regardless of the details discussed above, the fact that the narrow emission lines disappear after a few days—a defining characteristic of this class of events—provides a straightforward way to estimate the radial extent of the dense CSM. Combined with empirical expansion speeds, this can inform the timescale for the pre-SN mass loss by the progenitor. Whether the CSM is obliterated by the forward shock or enveloped by the SN photosphere, the narrow lines should disappear from the spectrum.

Narrow lines disappear after 1–2 days in our PEPSI spectra, and the intermediate-width lines disappear after 3–4 days. We assume that our first spectrum on May 21 was taken 2.6 days after explosion, so this means that the narrow lines disappear in 3.6–4.6 days, and the intermediate-width components (except $H\alpha$) disappear after 5.6–6.6 days. These timescales can be used to constrain the properties of the CSM.

In these early phases, we adopt an expansion speed for the SN ejecta photosphere of $10,000 \text{ km s}^{-1}$. The speed may be a bit

slower as time goes on, and the fastest ejecta are faster than this, but this assumption is sufficient for a rough estimate. At this speed, the relevant radius corresponding to the disappearance of the narrow components on day 3.6 is $R = vt = (3\text{--}5) \times 10^{14} \text{ cm}$, or about 20–30 au. This is only 5–10 R_* for a typical RSG. The corresponding timescale of the pre-SN mass ejection depends, of course, on the expansion speed of the CSM; i.e., $t_{\text{preSN}} = t_{\text{obs}} \times (v_{\text{CSM}}/v_{\text{SN}})$. For CSM produced by a normal RSG wind speed of $10\text{--}20 \text{ km s}^{-1}$, the CSM would have been ejected 5–10 yr before explosion. For a faster CSM expansion speed corresponding to the observationally inferred expansion speed of 115 km s^{-1} (see Figure 9), however, the pre-SN timescale for mass ejection is more like 0.9–1.5 yr.

Which one of these is correct returns us to the ambiguous question of whether the CSM is aspherical and if it has already been radiatively accelerated by the time of our first PEPSI spectrum on day 2.6. A timescale of 5–10 yr, expected for a normal slow RSG wind speed, does not match any expected timescale for late nuclear burning, but it is similar to the observationally inferred timescales for some SNe IIn (Smith 2017). We should not, however, necessarily expect a phase of extreme pre-SN mass loss to behave like a normal RSG wind. On the other hand, a pre-SN ejection timescale of ~ 1 yr, derived from the observed CSM speed, agrees well with the expected time for Ne or O burning. This agreement may favor instabilities in late Ne or O burning as the culprit for triggering the extreme pre-SN mass loss for SN 2023ixf. However, recent studies suggest that wave driving on its own may be unlikely to drive severe mass loss, instead being more likely to inflate the star’s envelope (Leung & Fuller 2020). As proposed by Smith & Arnett (2014), however, this type of sudden pre-SN swelling may trigger severe and asymmetric mass loss in binary systems.

4.4. Intermediate-width Features: Fading Away, Not Broadening

As noted above, the intermediate-width components of emission last longer than the narrow lines, which fade after 1–2 days. This is especially true of $H\alpha$, which persists for at least a week after explosion as a strong, intermediate-width P Cygni line. The intermediate-width emission component of $H\alpha$ disappears after another week or so, being gone by day 17.6 (gray spectrum in Figure 7). Unlike $H\alpha$, the intermediate-width components of the higher-ionization lines (He II, C IV, N IV) do not develop any P Cygni absorption features before they vanish after a few days. Why does this happen?

One reason for high-ionization lines to fade is recombination of the gas. We noted above, however, that as the N IV and C IV lines fade and disappear, we do not see a corresponding increase in strength of N III and C III lines. Also, although He I $\lambda 5876$ (only seen as an intermediate-width component) does increase in strength as He II fades, it never gets very strong, and it has disappeared again by day 17.7 (Figure 3(b)). Thus, even though we do see some evidence of recombination and cooling in the post-shock CDS (from $H\alpha$ P Cygni absorption and the increasing He I emission), recombination is not the primary explanation for the disappearance of the N IV and C IV lines.

Another reason why the intermediate-width emission from the post-shock shell might fade would be if the SN ejecta that feed the reverse shock are able to accelerate the shock front, essentially obliterating the slower moving post-shock gas as it is swept up to become part of the fast SN ejecta moving at

5000–10,000 km s⁻¹. In this case, we would expect the intermediate-width lines to broaden from 1000 to 5000 km s⁻¹ or more as they fade. This is not what the observational data show either. Instead, the intermediate-width components stay at about the same width or even become slightly narrower as they fade away. Importantly, on days 7.6 and 8.4, when the high-ionization lines have vanished, the P Cygni absorption seen in H α and He I still maintains the same slower speeds of 500–1300 km s⁻¹. This directly contradicts the idea that the post-shock shell is getting faster. We therefore find it unlikely that the CSM interaction signatures fade because the post-shock shell is accelerated and incorporated into the SN ejecta.

One last possibility arises if the CSM is significantly asymmetric, as in a case where the CSM is primarily equatorial. As noted above, the shock front that crashes into the densest material in the equator will be decelerated by the CSM. However, in other directions with much less dense CSM, the SN ejecta will expand unimpeded. Since the CSM here is found at radii of 20–30 au, whereas the SN photosphere will eventually reach a radius of around 100 au, the slower CSM interaction regions in the equatorial zones can be engulfed by the SN ejecta and hidden inside the SN photosphere. The opaque SN ejecta will wrap around the disk, if the disk is slow and thin enough. Even if the SN ejecta do not completely engulf the disk, it may be hidden from observers, as discussed in detail previously by Smith et al. (2015), and invoked as the explanation for the bizarre behavior of iPTF14hls (Andrews & Smith 2018). In this scenario, the CSM interaction zone with its relatively slow CDS may still be there, but its emission is blocked from our view or completely thermalized by the surrounding optically thick SN ejecta. There are observed cases where the CSM interaction persists while it is hidden beneath the photosphere, and signatures of strong CSM interaction reappear when the recombination photosphere recedes (i.e., after the plateau drops), as in PTF11iqb, iPTF14hls, SN 1993J, and SN 1998S (Matheson et al. 2000; Pozzo et al. 2004; Smith et al. 2015, 2017; Andrews & Smith 2018). On the other hand, if the asymmetric CSM has a low-enough total mass, it may indeed get obliterated and incorporated into the fast SN ejecta during the time when it is hidden beneath the photosphere, yielding little or no lingering CSM interaction signatures after the photosphere recedes. It will be interesting to see what happens after SN 2023ixf fades from its plateau and/or enters its nebular phase in a few months.

Note that this scenario where the CSM interaction region is engulfed by the SN photosphere only works if the CSM is highly asymmetric. Of the various pre-SN ejection mechanisms related to late-phase nuclear burning mentioned in the introduction (wave driving, super-Eddington winds, etc.), only pre-SN binary interaction triggered by envelope inflation (Smith & Arnett 2014) is necessarily expected to produce strong asymmetry in the CSM. This may turn out to be an important clue to the pre-SN mass loss.

Overall, the observational data seem to favor a scenario where the narrow lines fade and disappear mostly because the slow-moving CSM is swept up by the shock and accelerated, or even occulted. The intermediate-width components that are emitted by this shocked and accelerated CSM disappear a few days later because they are engulfed by and hidden inside the SN photosphere, and not because they are accelerated to the same speed as the SN ejecta, or because the ionized CSM

recombines. Engulfing the CSM interaction region rather than accelerating to the same speed as the ejecta requires that the CSM is asymmetric, as noted above, and probably indicates that we are observing the SN from some mid-latitude direction that is offset from the equatorial plane. This, in turn, is also consistent with the lack of any narrow P Cygni features in any of the high-resolution PEPSI spectra. This lack of narrow P Cygni absorption suggests asymmetry in the CSM because the slow CSM is not seen in absorption along our line of sight to the SN continuum photosphere, even though it is clearly seen in emission. This is only possible if the CSM is not spherical.

Although we argue that the CSM is asymmetric in the case of SN 2023ixf based on the observational behavior of the narrow and intermediate-width lines, this may not necessarily be the case for all SNe II with fleeting CSM interaction. It would be interesting to determine what fraction of these events show evidence of aspherical mass ejection shortly before explosion, and how many seem consistent with spherical CSM. This may help elucidate what role binary interaction may play in ejecting the mass, or shaping the mass ejected by some other mechanism.

4.5. Noteworthy Things We Do Not See

Here, we briefly comment on a few things that we do *not* see in the PEPSI spectra of SN 2013ixf, but which have been seen in early spectra of some other SNe II with fleeting signs of CSM interaction. These may help us to understand how SN 2023ixf fits into the observed diversity of this phenomenon.

1. Except for very weak and narrow components on day 2.6, we do not detect lines like the C III and N III blend in the “W-R bump” just to the blue side of He II $\lambda 4686$, or strong emission from narrow He I that has been seen in other early spectra of SN 1998S, PTF11iqb, 2013cu, and others (Gal-Yam et al. 2014; Shivvers et al. 2015; Smith et al. 2015).
2. We do not detect a broad emission feature near $\lambda 4600$ at any epoch. This broadened feature has been seen in several SNe II-P with fleeting CSM interaction signatures (Quimby et al. 2007; Bullivant et al. 2018; Hosseinzadeh et al. 2018; Andrews et al. 2019; Soumagnac et al. 2020; Hosseinzadeh et al. 2022; Pearson et al. 2023), and is often attributed to broad blueshifted He II $\lambda 4686$ emission from fast (5000–10,000 km s⁻¹) SN ejecta crossing the reverse shock, or a blend of He II $\lambda 4686$ with several other ionized features in the region. On the other hand, very broad features may be deemphasized by the continuum normalization in these cross-dispersed spectra if a faint broad feature crosses more than one echelle order, so the low-resolution spectra may be more informative about this broad He II feature.
3. Importantly, as noted above, we see no evidence for narrow P Cygni (or any) narrow absorption from unshocked CSM. While narrow absorption features can easily be lost in low-resolution spectra when they are seen next to a strong narrow emission feature, they are easily detected in echelle spectra (Smith & Andrews 2020). The absence of this absorption in SN 2023ixf may indicate that its slow and dense CSM is not seen along our line of sight to the continuum photosphere, requiring that the CSM has a nonspherical geometry. This would allow it to be seen in emission out of our line of sight, but not in absorption.

5. Summary and Conclusions

We present a series of high-resolution echelle spectra of the recent SN 2023ixf in M101. These provide an unprecedented record of the high-resolution emission-line evolution in an SN II with early signs of CSM interaction with an almost nightly cadence. These spectra reveal rapid evolution in the strength and profile shape of narrow and intermediate-width emission lines associated with CSM interaction. Here is a summary of the main observational results:

1. As in other SN of this class, we detect strong narrow and intermediate-width emission from $H\alpha$ and high-ionization lines such as He II, C IV, and N IV. Unlike several other SNe of this class, however, SN 2023ixf does not show strong emission from lower-ionization species like He I or C III/N III, which can be very strong in these objects. These lines are seen, but they are very weak and limited in time during our observational window.
2. All narrow line components fade quickly in 1–2 days from our first observation (which is a time period of 2–4 days post-explosion), and the intermediate-width components of high-ionization lines linger for another 1–2 days before fading from the spectrum.
3. All narrow emission components show a pronounced blueshift in the earliest epochs. The blueshift is understood as resulting from a combination of the light travel time effects and occultation of the far side of the CSM by the photosphere. However, the amount of blueshift and the width of the narrow component depend on both the time and on the ionization level of the line. Higher-ionization lines are broader and more blueshifted than lower-ionization lines in our first epoch, and this difference with ionization level diminishes after a day with all lines showing roughly the same width and blueshift as the higher-ionization species. This requires either acceleration of the innermost dense CSM, or asymmetric CSM.
4. The $H\alpha$ wings in our first epoch are consistent with electron scattering wings (i.e., they are well fit by a symmetric Lorentzian shape, with a centroid that has a similar blueshift as the narrow component). However, this changes after 1–2 days. $H\alpha$ and He I lines develop intermediate-width P Cygni absorption, requiring that the broadening of these lines after the first day or two is tracing kinematic expansion and is not due only to electron scattering. The P Cygni absorption indicates expansion speeds of 700–1300 km s⁻¹, tracing CSM that has been swept up in to the post-shock shell.
5. As the intermediate-width components fade, the observed velocities do not increase. The P Cygni absorption, in particular, remains steady at <1300 km s⁻¹. This requires that the CSM interaction signatures are not fading because the post-shock gas is getting accelerated and incorporated into the fast SN ejecta. Instead, the CSM interaction region is likely asymmetric and gets engulfed and hidden by the SN photosphere.
6. Although the narrow components are easily resolved in our echelle spectra, none of our spectra show narrow P Cyg absorption from dense pre-shock CSM along our line of sight to the continuum photosphere. This may require that the CSM is asymmetric.

7. The width of the narrow $H\alpha$ component indicates a CSM expansion speed of about 115 km s⁻¹, and this is seen in our first epoch before the $H\alpha$ appears to get accelerated to the same blueshift and width as the higher-ionization lines. This expansion speed is 5–10 times faster than a normal RSG wind.
8. The disappearance of the CSM interaction signatures after a few days suggests that the CSM is confined to a relatively compact radius of 20–30 au (or $\lesssim 10^{14.7}$ cm). This radius, combined with its observed expansion speed of 115 km s⁻¹, implies that the CSM was ejected roughly 1 yr before core collapse.

Altogether, we find several clues that the confined CSM of SN 2023ixf is asymmetric. We interpret the evolution of the line profiles as indicating that the asymmetric CSM interaction region is engulfed by the SN photosphere (e.g., Smith et al. 2015). While the narrow lines may weaken because the pre-shock gas is accelerated and incorporated into the post-shock shell, the resulting intermediate-width lines are hidden from view behind the SN photosphere, rather than the high-ionization lines fading away, because the shocked shell is accelerated or because the gas recombines. While the inferred timescale for creating SN 2023ixf’s pre-SN CSM is about a year (which suggests an instability during Ne or O burning), the implied asymmetry in the CSM points to a scenario where pre-SN inflation during Ne or O burning will instigate binary interaction that ejects mass into a disk or torus. Thus, CSM interaction may continue to occur as SN ejecta hit the engulfed CSM, but it may be hidden from our view. Depending on the mass of the CSM, CSM interaction signatures may reappear after SN 2023ixf drops from its plateau when the recombination photosphere recedes again.







Acknowledgments

We thank an anonymous reviewer for comments that improved the paper. For help with obtaining and reducing the spectra, we thank LBT staff members including Alex Becker, Jennifer Power, and director Joe Shields. Some of these LBT/PEPSI spectra were obtained as part of a pre-approved program called AZTEC (Arizona Transient Exploration and Characterization), but some resulted from Director’s Discretionary Time and Engineering time, which allowed a nearly nightly cadence during a critical time period. The LBT is an international collaboration among institutions in the United States, Italy, and Germany. LBT Corporation partners are: The University of Arizona on behalf of the Arizona university system; Istituto Nazionale di Astrofisica, Italy; LBT Beteiligungsgesellschaft, Germany, representing the Max-Planck Society, the Astrophysical Institute Potsdam, and Heidelberg University; The Ohio State University, and The Research Corporation, on behalf of The University of Notre Dame, University of Minnesota and University of Virginia.

Time domain research by D.J.S. and team is supported by NSF grants AST-1821987, 1813466, 1908972, and 2108032, and by the Heising-Simons Foundation under grant No. 20201864. This publication was made possible through the support of an LSSTC Catalyst Fellowship to K.A.B., funded through grant 62192 from the John Templeton Foundation to LSST Corporation. The opinions expressed in this publication are those of the authors and do not necessarily reflect the views of LSSTC or the John Templeton Foundation.

Facility:LBT (PEPSI).

ORCID iDs

Nathan Smith  <https://orcid.org/0000-0001-5510-2424>
 Jeniveve Pearson  <https://orcid.org/0000-0002-0744-0047>
 David J. Sand  <https://orcid.org/0000-0003-4102-380X>
 Ilya Ilyin  <https://orcid.org/0000-0002-0551-046X>
 K. Azalee Bostroem  <https://orcid.org/0000-0002-4924-444X>
 Griffin Hosseinzadeh  <https://orcid.org/0000-0002-0832-2974>
 Manisha Shrestha  <https://orcid.org/0000-0002-4022-1874>

References

- Andrews, J. E., & Smith, N. 2018, *MNRAS*, **477**, 74
 Andrews, J. E., Sand, D. J., Valenti, S., et al. 2019, *ApJ*, **885**, 43
 Arnett, W. D., & Meakin, C. 2011, *ApJ*, **741**, 33
 Beasor, E. R., Davies, B., Smith, N., et al. 2020, *MNRAS*, **492**, 5994
 Beasor, E. R., & Smith, N. 2022, *ApJ*, **933**, 41
 Benetti, S., Patat, F., Turatto, M., et al. 1994, *A&A*, **285**, L13
 Bostroem, K. A., Pearson, J., & Shrestha, M. 2023, arXiv:2306.10119
 Bruch, R. J., Gal-Yam, A., Schulze, S., et al. 2021, *ApJ*, **912**, 46
 Bullivant, C., Smith, N., Williams, G. G., et al. 2018, *MNRAS*, **476**, 1497
 Chiosi, C., & Maeder, A. 1986, *ARA&A*, **24**, 329
 Chugai, N. N. 2001, *MNRAS*, **326**, 1448
 Chugai, N. N. 2019, *AstL*, **45**, 71
 Chugai, N. N., Blinnikov, S. I., Cumming, R. J., et al. 2004, *MNRAS*, **352**, 1213
 de Vaucouleurs, G., de Vaucouleurs, A., Corwin, H. G., et al. 1995, *yCat*, **7155**, 0
 Drout, M. R., Soderberg, A. M., Gal-Yam, A., et al. 2011, *ApJ*, **741**, 97
 Fuller, J. 2017, *MNRAS*, **470**, 1642
 Gal-Yam, A., Arcavi, I., Ofek, E. O., et al. 2014, *Natur*, **509**, 471
 Garnavich, P. M., & Ann, H. B. 1994, *AJ*, **108**, 1002
 Gräfener, G., & Vink, J. S. 2016, *MNRAS*, **455**, 112
 Groh, J. H. 2014, *A&A*, **572**, L11
 Heger, A., Fryer, C. L., Woosley, S. E., Langer, N., & Hartmann, D. H. 2003, *ApJ*, **591**, 288
 Hosseinzadeh, G., Farah, J., Shrestha, M., et al. 2023, *ApJL*, **953**, L16
 Hosseinzadeh, G., Kilpatrick, C. D., Dong, Y., et al. 2022, *ApJ*, **935**, 31
 Hosseinzadeh, G., Valenti, S., McCully, C., et al. 2018, *ApJ*, **861**, 63
 Ilyin, I. V. 2000, PhD thesis, University of Oulu
 Jacobson-Galán, W. V., Dessart, L., Jones, D. O., et al. 2022, *ApJ*, **924**, 15
 Jacobson-Galán, W. V., Dessart, L., Margutti, R., et al. 2023, *ApJL*, **954**, L42
 Jencson, J. E., Pearson, J., Beasor, E. R., et al. 2023, *ApJL*, **952**, L30
 Khazov, D., Yaron, O., Gal-Yam, A., et al. 2016, *ApJ*, **818**, 3
 Kilpatrick, C. D., Foley, R. J., Jacobson-Galán, W. V., et al. 2023, *ApJL*, **952**, L23
 Leonard, D. C., Filippenko, A. V., Barth, A. J., & Matheson, T. 2000, *ApJ*, **536**, 239
 Leung, S.-C., & Fuller, J. 2020, *ApJ*, **900**, 99
 Matheson, T., Filippenko, A. V., Ho, L. C., Barth, A. J., & Leonard, D. C. 2000, *AJ*, **120**, 1499
 Niemela, V. S., Ruiz, M. T., & Phillips, M. M. 1985, *ApJ*, **289**, 52
 Paczyński, B. 1971, *ARA&A*, **9**, 183
 Pearson, J., Hosseinzadeh, G., Sand, D. J., et al. 2023, *ApJ*, **945**, 107
 Perley, D. A., Gal-Yam, A., Irani, I., & Zimmerman, E. 2023, *TNSAN*, **119**, 1
 Pledger, J. L., & Shara, M. M. 2023, *ApJL*, **953**, L14
 Podsiadlowski, P., Joss, P. C., & Hsu, J. J. L. 1992, *ApJ*, **391**, 246
 Poznanski, D., Prochaska, J. X., & Bloom, J. S. 2012, *MNRAS*, **426**, 1465
 Pozzo, M., Meikle, W. P. S., Fassia, A., et al. 2004, *MNRAS*, **352**, 457
 Puls, J., Vink, J. S., & Najarro, F. 2008, *A&ARv*, **16**, 209
 Quataert, E., & Shiode, J. 2012, *MNRAS Lett.*, **423**, L92
 Quimby, R. M., Wheeler, J. C., Höflich, P., et al. 2007, *ApJ*, **666**, 1093
 Salamanca, I., Terlevich, R. J., & Tenorio-Tagle, G. 2002, *MNRAS*, **330**, 844
 Sana, H., de Mink, S. E., de Koter, A., et al. 2012, *Sci*, **337**, 444
 Schlafly, E. F., & Finkbeiner, D. P. 2011, *ApJ*, **737**, 103
 Schlegel, E. M. 1990, *MNRAS*, **244**, 269
 Shiode, J. H., & Quataert, E. 2014, *ApJ*, **780**, 96
 Shiode, J. H., Quataert, E., Cantiello, M., & Bildsten, L. 2013, *MNRAS*, **430**, 1736
 Shivvers, I., Groh, J. H., Mauerhan, J. C., et al. 2015, *ApJ*, **806**, 213
 Smith, N. 2014, *ARA&A*, **52**, 487
 Smith, N. 2017, in *Handbook of Supernovae*, ed. A. W. Alsabti & P. Murdin (Berlin: Springer), 403
 Smith, N., & Andrews, J. E. 2020, *MNRAS*, **499**, 3544
 Smith, N., & Arnett, W. D. 2014, *ApJ*, **785**, 82
 Smith, N., Chornock, R., Li, W., et al. 2008, *ApJ*, **686**, 467
 Smith, N., Chornock, R., Silverman, J. M., Filippenko, A. V., & Foley, R. J. 2010, *ApJ*, **709**, 856
 Smith, N., Kilpatrick, C. D., Mauerhan, J. C., et al. 2017, *MNRAS*, **466**, 3021
 Smith, N., Li, W., Filippenko, A. V., & Chornock, R. 2011, *MNRAS*, **412**, 1522
 Smith, N., Mauerhan, J. C., Cenko, S. B., et al. 2015, *MNRAS*, **449**, 1876
 Smith, N., & Owocki, S. P. 2006, *ApJL*, **645**, L45
 Soraisam, M., Matheson, T., Andrews, J., et al. 2023, *TNSAN*, **139**, 1
 Soumagnac, M. T., Ganot, N., Irani, I., et al. 2020, *ApJ*, **902**, 6
 Strassmeier, K. G., Ilyin, I., & Steffen, M. 2018, *A&A*, **612**, A44
 Sundqvist, J. O., Björklund, R., Puls, J., & Najarro, F. 2019, *A&A*, **632**, A126
 Tartaglia, L., Sand, D. J., Groh, J. H., et al. 2021, *ApJ*, **907**, 52
 Terreran, G., Jacobson-Galán, W. V., Groh, J. H., et al. 2022, *ApJ*, **926**, 20
 Trundle, C., Kotak, R., Vink, J. S., & Meikle, W. P. S. 2008, *A&A*, **483**, L47
 Woosley, S. E. 2017, *ApJ*, **836**, 244
 Woosley, S. E., & Heger, A. 2015, *ApJ*, **810**, 34
 Wu, S., & Fuller, J. 2021, *ApJ*, **906**, 3
 Yoon, S.-C., & Cantiello, M. 2010, *ApJL*, **717**, L62